

## Effects of skull properties on transcranial focused ultrasound transmission

Han Li,<sup>1</sup> Isla Barnard,<sup>1</sup> Tyler Halliwell,<sup>1</sup> Xinyu Zhang,<sup>2</sup> Andreas Melzer,<sup>2</sup> and Zhihong Huang<sup>1,2</sup>

<sup>1</sup> *School of Science and Engineering, University of Dundee, Dundee, DD1 4HN, UK*

<sup>2</sup> *School of Medicine, University of Dundee, Dundee, DD1 9SY, UK*

ABSTRACT: Transcranial focused ultrasound can deliver energy to the brain in a minimally invasive manner for a variety of clinical applications. However, acoustic inhomogeneities within the skull cause significant wave interactions, leading to difficulties in predicting the energy delivered to the target. We present a comprehensive examination of intracranial acoustic fields generated by focused ultrasound transducers and assess the characteristics of cranial bone that affect acoustic transmission. Acoustic field maps were generated at 88 regions of interest across 10 historical and 2 Thiel-embalmed human skull specimens with sonication at frequencies of 220 kHz, 650 kHz, and 1000 kHz. The average peak pressure attenuation was  $3.1 \pm 1.4$  dB,  $9.0 \pm 1.7$  dB, and  $14.6 \pm 4.1$  dB, and the average power attenuation was  $5.0 \pm 2.4$  dB,  $14.9 \pm 3.2$  dB, and  $24.1 \pm 6.3$  dB, respectively. The effect of skull thickness, skull density ratio, and skull curvature on intracranial peak pressure and power was investigated and linear fits produced. Our results demonstrate that Thiel-embalmed samples fall within the confidence intervals of fits for historical samples. The effects of angulation and spacing between the transducer and the skull were also investigated. Results indicate that wave superposition resulting from skull and transducer spacing could lead to a 30-40% uncertainty in peak recorded intracranial pressure.

## I. INTRODUCTION

Transcranial Low Intensity Focused Ultrasound (LIFU) for neuromodulation is a promising and rapidly developing technology<sup>1-6</sup> with the ability to probe motor and cognitive functional connectivity in the brain in a non-invasive reversible manner.<sup>7-11</sup>

Transcranial LIFU offers several advantages over established non-invasive forms of neuromodulation. LIFU affords the possibility of neuromodulating brain tissue with the spatial precision required to translate to clinically meaningful targets.<sup>2,5</sup> LIFU also has the potential to neuromodulate deep brain structures,<sup>3,6</sup> whereas established modalities, such as transcranial magnetic stimulation (TMS) can reach only cortical regions and precision targeting is not possible.

Though the mechanisms underlying this have been the source of debate, it is recognised that LIFU temporarily disrupts brain circuit function by altering the state of ion channels in neurons.<sup>12</sup> Recent *in-vitro* studies indicate that calcium-permeable ion channels require a continuous excitation for 200 ms and a constant 15 W/cm<sup>2</sup> energy deposition to activate a neuronal response,<sup>12</sup> though *in-vivo* parameters are yet to be determined.

However, analogous to difficulties surrounding utilising ultrasound for brain imaging, it is a challenge to deliver LIFU through the skull, into the brain.<sup>2</sup> The skull significantly attenuates the acoustic field, so target engagement (ensuring the intended target is stimulated while avoiding off-target unintended neuromodulation) remains a challenge.

Previous studies have extensively explored and characterized the effects of human skulls on acoustic transmission using pulses of a few cycles, revealing a strong inverse relationship between the acoustic pressure attenuation and skull thickness, as well as ultrasound frequency.<sup>13-19</sup> During transcranial LIFU treatment, pulse patterns contain several hundred cycles per pulse delivered, and as such would be considered to fall in the ‘continuous-wave’ regime in acoustics.

Such waveforms could introduce constructive or destructive interference at both the transducer-skull spacing and within the skull thickness. This may lead to different attenuation coefficient measurements compared with those obtained via a short-pulsed waveform.<sup>20–22</sup>

Ultrasound simulation software plays a crucial role in predicting the intracranial acoustic field.<sup>23</sup> Accurate representation of the inherent heterogeneity of the skull and associated acoustic properties, i.e., medium density, speed of sound, and attenuation coefficient, are vital for developing simulations that produce meaningful results.

This study focuses on developing methodology to assess the significance of the physical properties of the skull, and of skull-transducer placement on focused ultrasound transmission. By comparing the acoustic field measurements in the free-field to that in the presence of a skull, an assessment is made of the impact of the skull thickness, skull density ratio (SDR) and the degree of skull curvature, as well as the skull-transducer angulation and spacing on the resulting intracranial acoustic field.<sup>24</sup>

## **II. MATERIALS AND METHODS**

### **A. Skull selection and physical properties**

In this experiment, 10 historical human skulls (8 calvaria and 2 half-skulls) and 2 Thiel-embalmed<sup>25</sup> human calvaria were sourced from the Centre for Anatomy and Human Identification (CAHID). The historical specimens were selected based on variation in size and shape from a pool of approximately 200 available skulls. Although the provenance of the collection is not known, the extensive range and variability suggest a broad representation of ages and sexes.

The Thiel calvaria samples provided came from Thiel soft embalmed cadavers (most of the donors are between the ages of 75 and 95). These samples retain the elasticity and feel of living tissue, with both scalp and dura intact. The donations were handled confidentially and the

procedures involving of the Thiel calvaria has been strictly following the Scottish Anatomy and the Human Tissue Act.<sup>26</sup>

For each half skull, 4 regions of interest (ROIs) were selected. For the calvaria samples (both historical and Thiel) these regions were mirrored across the medial line, giving 8 ROIs for each calvaria. This resulted in a total of 88 ROIs (72 in historical dry skulls and 16 in Thiel). FIG.1(a), details how regions of interest (ROI) are distributed across a half skull sample. To obtain structural and morphological information from the skulls, CT scans were obtained (GE Revolution EVO CT scanner; with in-plane spacing at 0.44 mm for both axes and slice thickness of 0.625 mm with 0.31 mm interval). Prior to CT scanning, ROIs were marked on each sample using metallic ball bearings to identify ROIs during image analysis. An example of the resulting ROI volume obtained from a CT scan is shown in FIG.1(b). This volume is used as an illustrative example throughout and is labeled as S1.

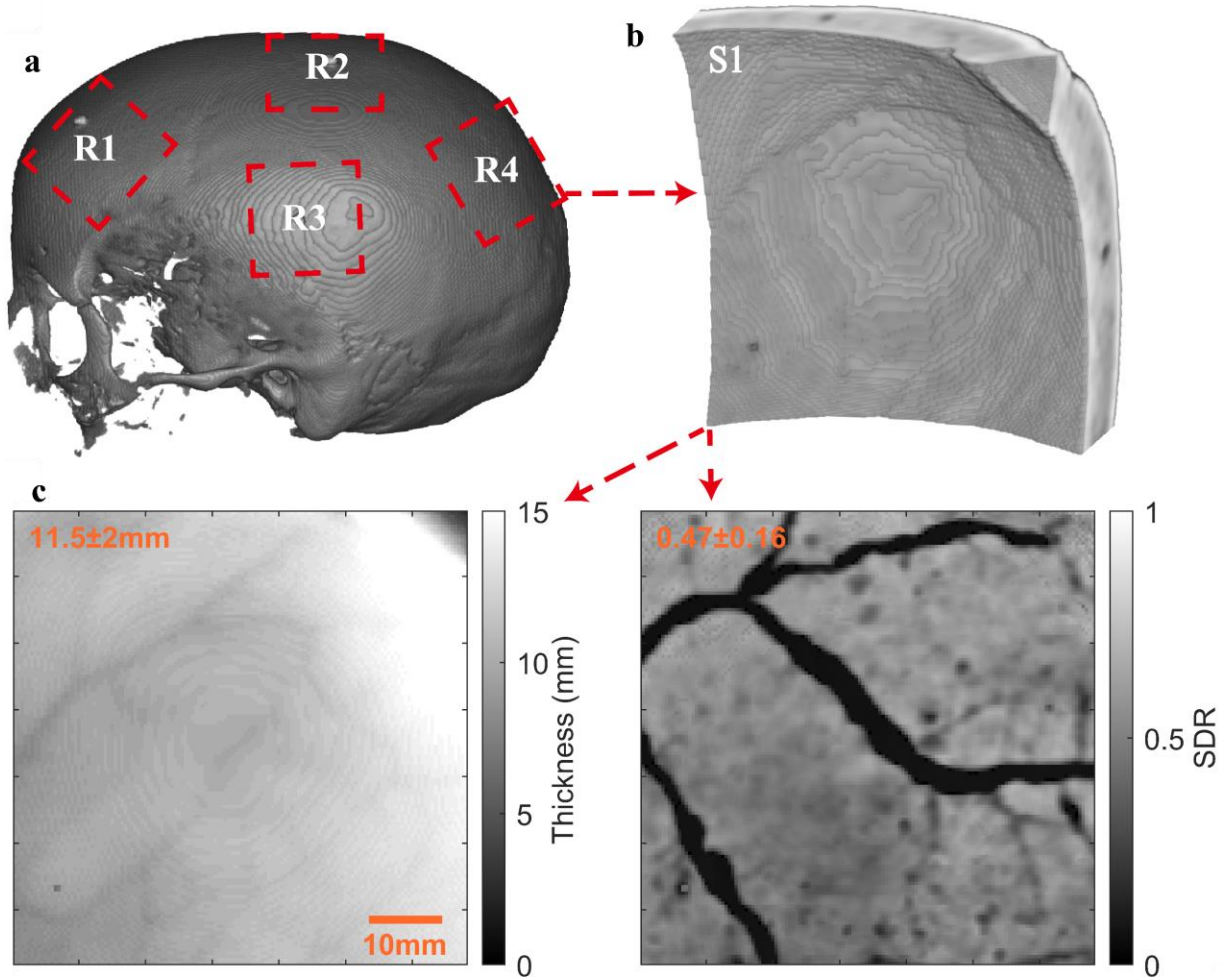


FIG.1. (Color online). A representative skull with Region of Interest (ROI) details. (a) ROI locations on a half skull. R1 is frontal bone, R2 superior parietal, R3 lateral parietal (partial temporal in some samples), and R4 is posterior parietal bone. (b) The CT volume of an example ROI (60 mm by 60 mm surface area) labeled throughout as S1, (c) Thickness and SDR map of S1. Average thickness and SDR are  $11.5 \pm 2.0$  mm, and  $0.47 \pm 0.16$ , respectively. The radius of curvature (RoC) of S1 is approximately 55.1 mm.

ROIs were characterized by thickness, skull density ratio (SDR) and radius of curvature (RoC), all obtained from analysis of the CT scans. The SDR is used as a screening and planning tool in MRI-guided focused ultrasound neurosurgery and is the ratio between the minimum and maximum

radiodensity;<sup>27</sup> which for skulls is a metric representing the ratio between trabecular and cortical bone.

To characterize the skulls, each CT scan was imported into MATLAB. A surface casting method (an extension to the ray-casting method<sup>28,29</sup> used to find SDR from a CT scan); that considers ultrasound insertion angle, was developed to calculate both the SDR and the thickness.

Each volume was defined by selecting an approximately 60 mm by 60 mm square region from the skull surface, with the ROI metallic marker at the center. Each segmented ROI was 136 voxels wide and 193 voxels long. The ROI marker was removed from the image; and the inner and outer surfaces were defined as the point where HU units reach 300 HU.

A straight line was drawn from each outer surface voxel to the inner surface. The length of each line times a cosine factor of the predicted sound insertion angle was calculated and averaged to give the average and standard deviation of the thickness for the ROI. The SDR was calculated based on the same principle (without angulation correction). To recover a realistic density for trabecular bone, a lower bound threshold was set to +100 HU. FIG.1(c) shows the corresponding thickness and SDR map of S1.

To determine the curvature of the ROI, the inner and outer surface of the ROI were fitted to a best-fit spherical surface. The average of the two curvatures was used as the metric to indicate RoC. The three characteristics of the grouped four regions data are presented in TABLE I.

TABLE I. The mean and standard deviation of skull region-specific parameters over all 88 ROIs tested.

	R1	R2	R3	R4
Thickness (mm)	7.7±2.6	6.4±1.9	5.8±1.9	8.0±2.3

SDR	$0.42 \pm 0.23$	$0.46 \pm 0.19$	$0.47 \pm 0.21$	$0.40 \pm 0.19$
RoC (mm)	$54.6 \pm 10.5$	$80.3 \pm 17.5$	$48.5 \pm 12.6$	$51.2 \pm 7.7$

## B. Experimental setup & acoustic measurements

Three single element focused ultrasound transducers with centre frequencies of 220 kHz, 650 kHz, and 1000 kHz, with identical diameters of 60 mm and focal lengths of 75 mm, (Precision acoustics, UK) were selected. Transducers were driven by approximately 0.5 ms sinusoidal waveform generated by a signal generator (Keysight, US), which produces peak negative pressure in the free-field of 0.06 MPa at 220 kHz, 0.25 MPa at 650 kHz, and of 0.35 MPa at 1000 kHz. A 1 mm needle hydrophone (Precision Acoustics, UK) was used to capture the acoustic signal. Prior to the experiment, hydrophone sensitivity and power measurement calibrations were performed in accordance with hydrophone characterization standards IEC 62127-1/2,<sup>30,31</sup> the transducer transmitted field measurement standard IEC 61828,<sup>32</sup> and the ultrasonic power measurement standards IEC 61689<sup>33</sup> and IEC 61161.<sup>34</sup>

The hydrophone was mounted on a three-dimensional motor stage (Velmex, US), and was positioned at the focal depth, pointing towards the transducer. The received signal was sampled at 40Mz by a PC oscilloscope (Picoscope, UK), and the waveform was reconstructed through a center frequency band-pass filter. Free-field mapping with a step resolution of 0.5 mm was performed as a reference for each frequency. The sizes of the transverse mapping planes were 30 mm by 30 mm (220 kHz) and 20 mm by 20 mm (for 650 kHz and 1000 kHz). The areas chosen sufficiently cover the full width half maximum (FWHM) beam area, and importantly are small enough to afford daily calibration prior to experimental data acquisition.

Prior to the experimental setup as shown in FIG. 2, each historical skull sample was degassed in a vacuum tank until no visible air bubbles escaped from the incised edge. The Thiel embalmed skulls were also degassed as above. Following degassing, Thiel skulls were vacuum sealed using an acoustically & visually transparent sealing bag (with tested transmission efficiency > 99%). Sealing prevented Thiel embalming fluid leaching from the sample into the water tank, and also prevented detachment of soft tissues from the skull caused by water ingress.

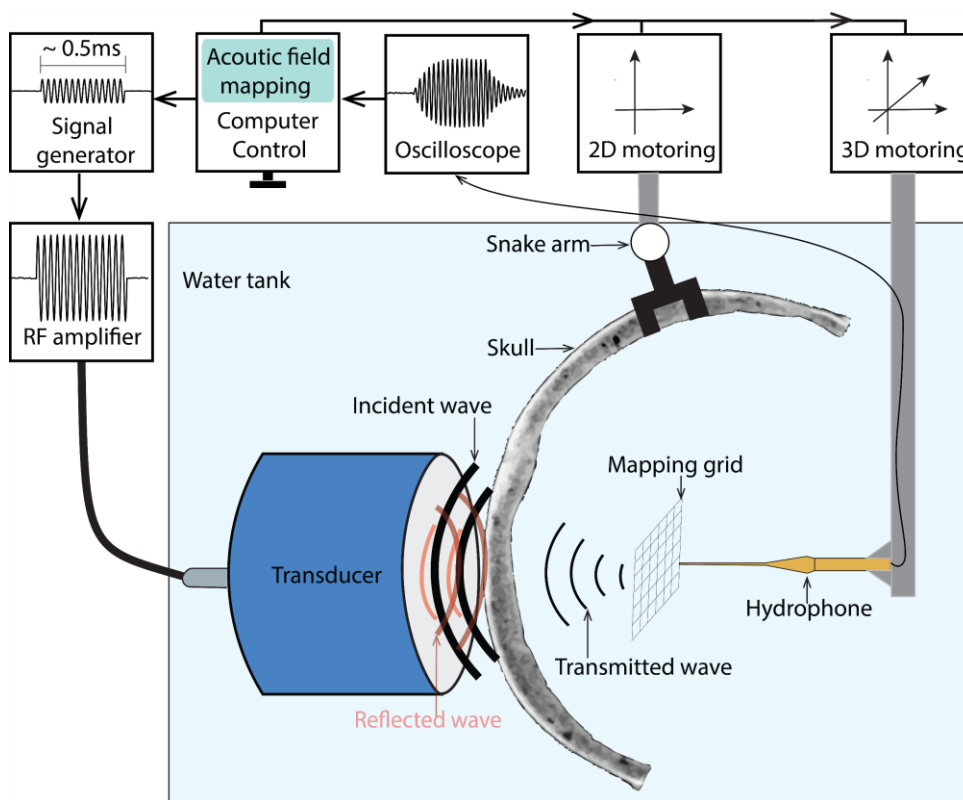


FIG. 2. (Color online). Experimental setup of the transcranial acoustic field measurement system.

The degassed skull was then clamped on a snake arm that can be locked in any position and which was fixed on a two-dimensional motoring stage, and positioned between the transducer and hydrophone.

To investigate the influence of the skull properties on the transmitted pressure and power level (and the sharpness of the focus), the position of all ROIs under testing were aligned to near-normal incidence, and were maneuvered approximately 10 mm from the transducer aperture. Acoustic field measurements were taken in the same position as the free-field mapping to capture skull-induced changes in the transmitted acoustic field.

To investigate the impact of transducer-skull spacing on the transmitted acoustic pressure level, using a single ROI, the gap between the skull and the transducer aperture was increased from 10 mm to 50 mm, in increments of 0.2 mm, and the pressure at the focal point was recorded. Using the 650 kHz transducer and a single ROI, the effect of angle between the transducer and the skull was also investigated. The relative angle was moved from 0° to 15°, then to 30°, and the resulting field was mapped with a step resolution of 0.5 mm along the beam axis. The corresponding pressure  $p$  at each sampling position and the total acoustic  $P_{HP}$  power can be calculated by using equation:<sup>32</sup>

$$P_{HP} = \iint \left( \overline{p(x, y)}^2 / \rho c \right) dydx, \quad p = U/M_f \quad (1)$$

Where  $U$  is the signal amplitude,  $M_f$  is the hydrophone sensitivity at transducer working frequency,  $\overline{p(x, y)}$  is the time averaged acoustic pressure at coordinate  $(x, y)$ ,  $\rho$  and  $c$  are the density and sound velocity of water (1000 kg/m<sup>3</sup> and 1480 m/s, respectively),  $dydx$  is the pixel area (assumed to be the square of the step-resolution). By integrating over the mapping area, we recover the  $P_{HP}$ ; the approximate total acoustic power transmitted through that area. The system control, data acquisition and data processing software were developed in-house in MATLAB, and the acoustic field aberration analysis was performed in SPSS V26.0.

### III. RESULTS

#### A. Acoustic field analysis

The scheme used to analyze the acoustic field is shown in FIG. 3, using volume S1 (FIG.1) as an example. In order to compare the transmitted acoustic field across 88 ROIs, the intracranial focal area was defined as the region where the pressure level above the -6 dB (half-maximum) and is shown in FIG. 3. (a) as the dashed circle on the maps.

As depicted in FIG. 3 (b) and (c), the aberration of the beam was further assessed by quantifying the normalized pressure-weighted phase errors between the intracranial focal area and the corresponding area projected onto the reference. The colorless grids represent the peak and ambient pressure fields in the free-field, and the acoustic fields transmitted through S1 were represented by the color grid. The full-cycle pressure vibration error compared to the free-field is shown in FIG. 3 (d).

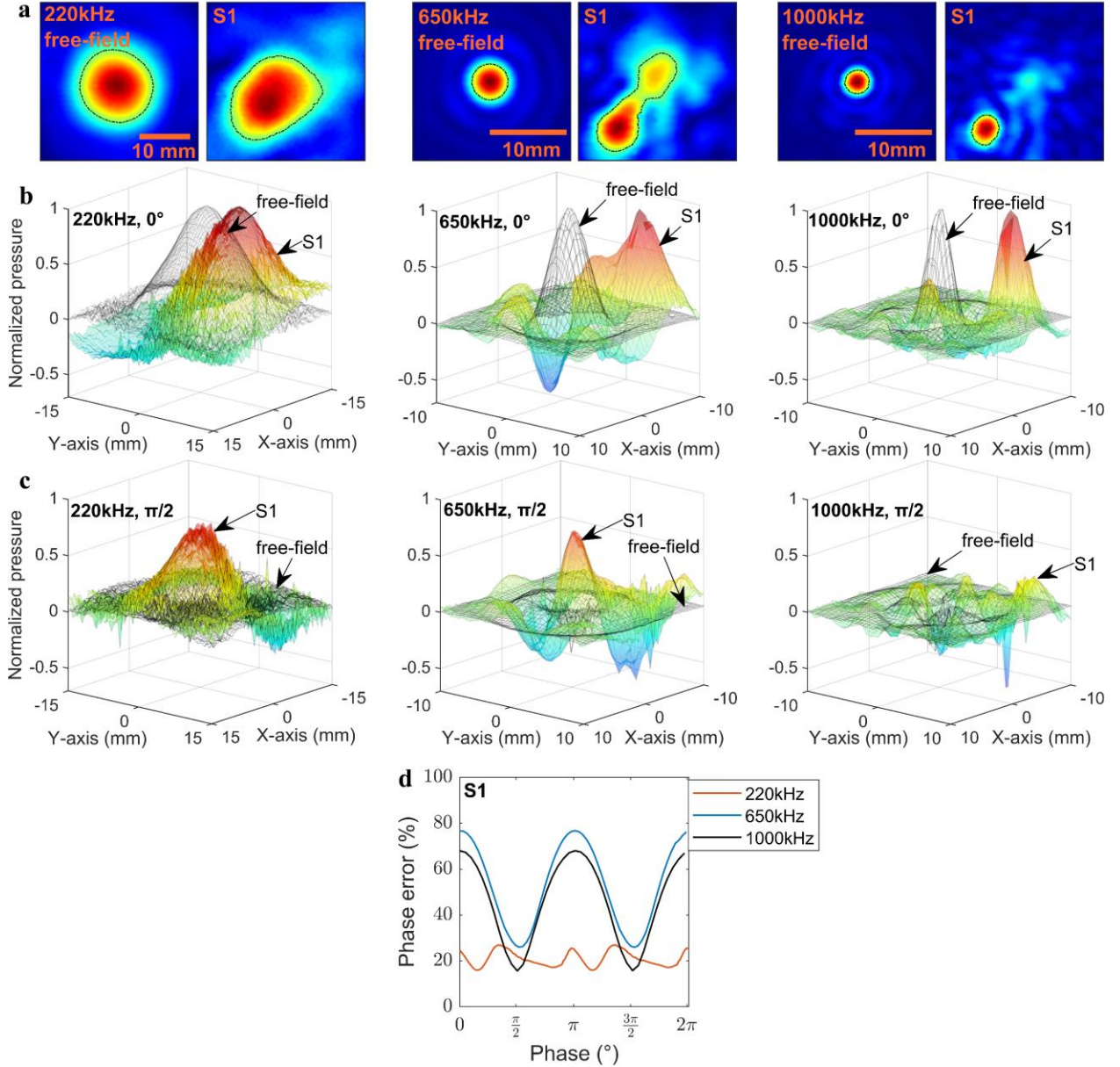


FIG. 3.(Color online). Acoustic field aberration analysis for the representative region S1 that was described in FIG.1. (a) Cross-sectional beam area pressure maps at the focal depths of the 220 kHz, 650 kHz and 1000 kHz transducers, produced at the focal depth in both free-field and with the presence of S1. (b) and (c) Color-less grids of three frequencies show a normalized pressure map at the focal depth in free-field at phase  $=0^\circ$  and  $\pi/2$ , respectively. The composed color images are those with the presence of S1. (d) The full vibration cycle phase errors of the pressure fields of S1 compared to the reference free-field were recorded at three frequencies.

As the representative field analysis for the S1 region shows, some field maps exhibited such severe acoustic field aberration that there was no meaningful focal point to identify. Such examples were systematically excluded from further analysis. To do so, all the field maps were manually inspected, and phase error was fitted to a logistic regression model to define the receiver operating characteristic curve. The calculated cut off phase error are 20.2%, 21.5% and 30.6% for 220 kHz, 650 kHz and 1000 kHz, respectively. The characteristics of the ROIs causing phase error beyond the cut off value were analyzed, and the two significant factors identified were found. These were the RoC of the ROI, and the degree of variation in thickness across the ROI. Thickness deviations of more than 2.0 mm at 220 kHz, more than 1.8 mm at 650 kHz and more than 1.3 mm at 1000 kHz; and all RoCs outside 30 mm and 100 mm were excluded. Averaged results from ROIs included (for historical skulls) are presented in TABLE II.

TABLE II. The average results of the three frequencies from included ROIs.

Averaged results from ROIs	220 kHz	650 kHz	1000 kHz
Normalized peak pressure (dB)	$-3.1 \pm 1.4$	$-9.0 \pm 1.7$	$-14.6 \pm 4.1$
Normalized power (dB)	$-5.0 \pm 2.4$	$-14.9 \pm 3.2$	$-24.1 \pm 6.3$
Normalized focal area	$1.1 \pm 0.2$	$1.3 \pm 0.1$	$1.5 \pm 0.2$

Phase error (%)	$15.2 \pm 5.1$	$15.4 \pm 5.3$	$23.8 \pm 11.2$
Focus shift (mm)	$2.1 \pm 1.6$	$0.9 \pm 0.4$	$0.7 \pm 0.4$

### B. Transcranial pressure and power level, and sharpness of the focus analysis

The results from included ROIs were aggregated, and fitted to a linear regression model, accompanied by a 95% confidence interval (CI), to demonstrate the correlation between the pressure and power level, as well as the sharpness of the focus, to the ROI thickness (FIG. 4), SDR (FIG. 5) and the RoC (FIG. 6) at the three frequencies.

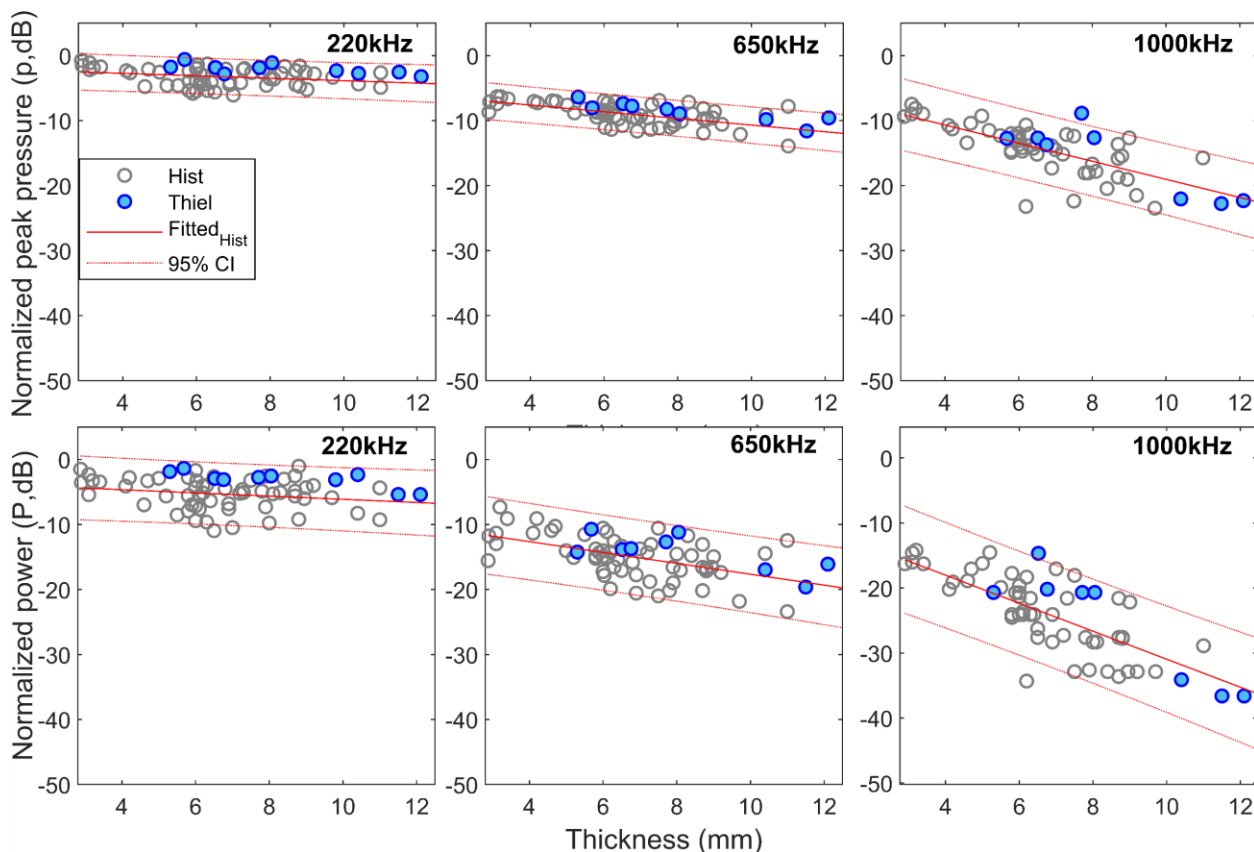


FIG. 4. (Color online). Skull thickness versus the normalized transcranial peak pressure level (dB), power level (dB) at three frequencies. The grey circles indicate are historical skull ROIs, and filled blue circles represent Thiel ROIs. The linear fit (plus 95 % confidence interval) to the historical ROI data is indicated as shown.

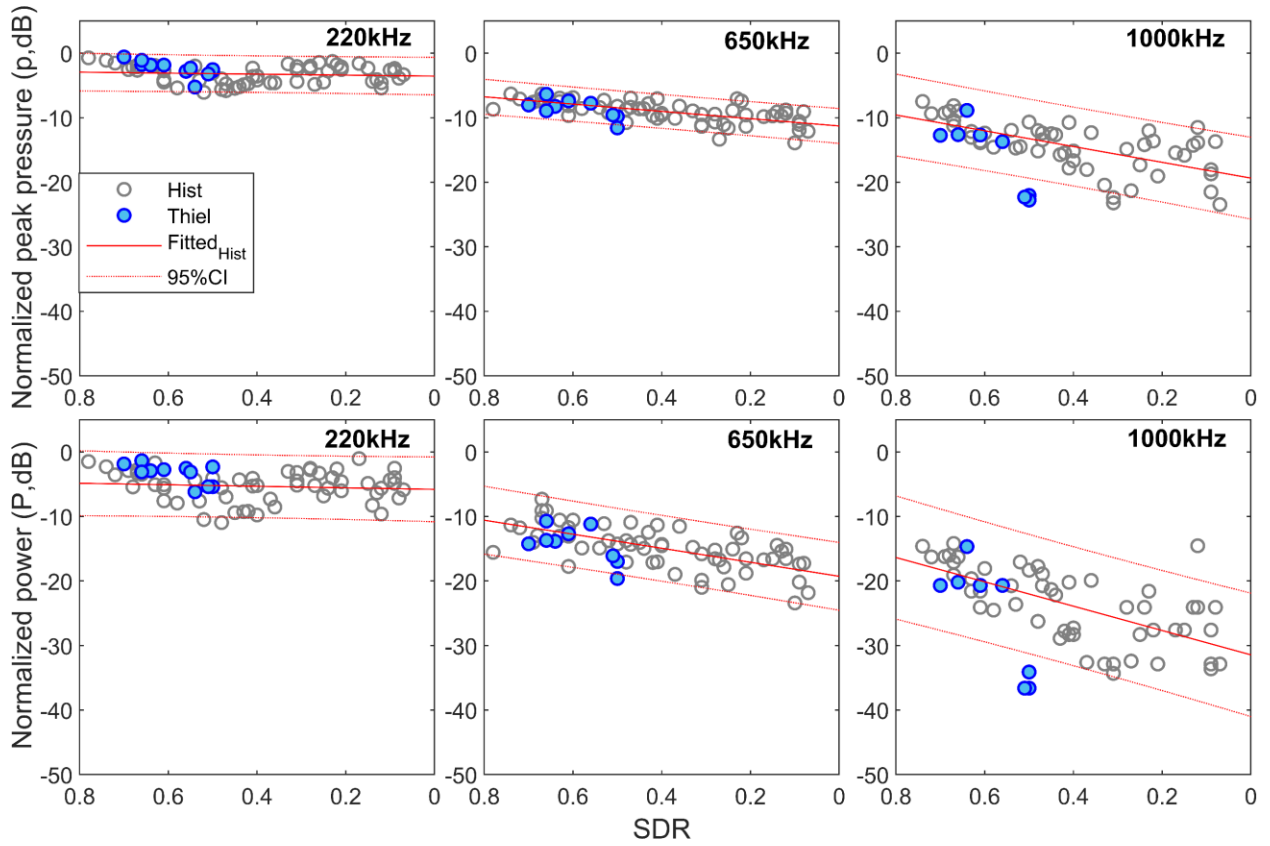


FIG. 5. (Color online). Skull SDR versus the normalized transcranial peak pressure level (dB) and power level (dB).

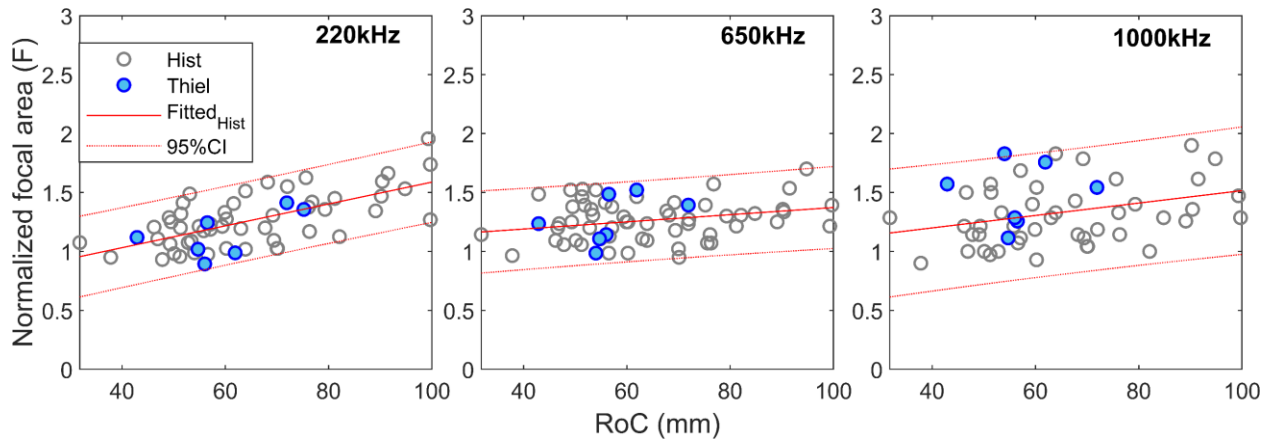


FIG. 6. (Color online). Skull ROI RoC versus the normalized focal area ( $F$ ) at three frequencies. The focal areas were normalized to the free-field reference- a larger ratio indicates a blurred focus, and a smaller ratio indicates a sharper focus.

### C. Transducer-skull spacing and placement angulation

During early testing of longer period sonication (dozens of cycles), a wave superposition effect started to be noticeable across the ROIs- an investigation is presented in FIG. 7.

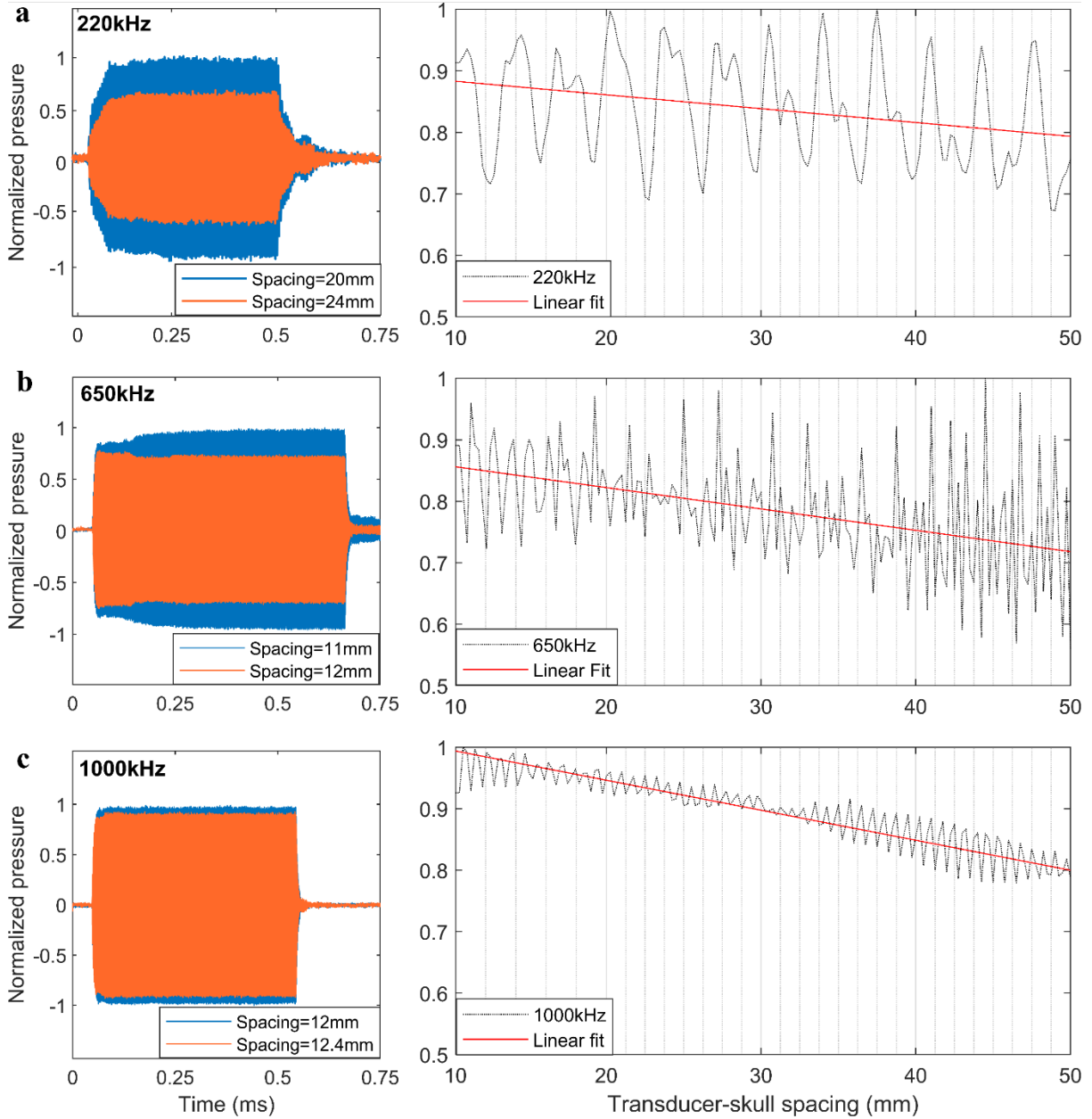


FIG. 7. Color online). Pressure variation at the intracranial focus along the increase of the transducer and representative skull (thickness of 3.2 mm, SDR of 0.65 and RoC of 70.0 mm) spacing at three frequencies and its waveform. (a-c) Waveform amplitude development at spacing approximately of 20 mm and 24 mm, 11 mm and 12 mm, 12 mm and 12.4 mm, and the pressure variation from 10 mm to 50 mm spacing at 220 kHz, 650 kHz, and 1000 kHz, respectively. The linear fitted red line showed the overall decreasing trend of the pressure along the spacing.

The effects of a skull piece (thickness of 6.2 mm, SDR of 0.50, and RoC of 56.1 mm) on the acoustic field at normal incidence at 650 kHz, and the impact of its placement angle and resulting field aberration was tested and is illustrated in FIG. 8.

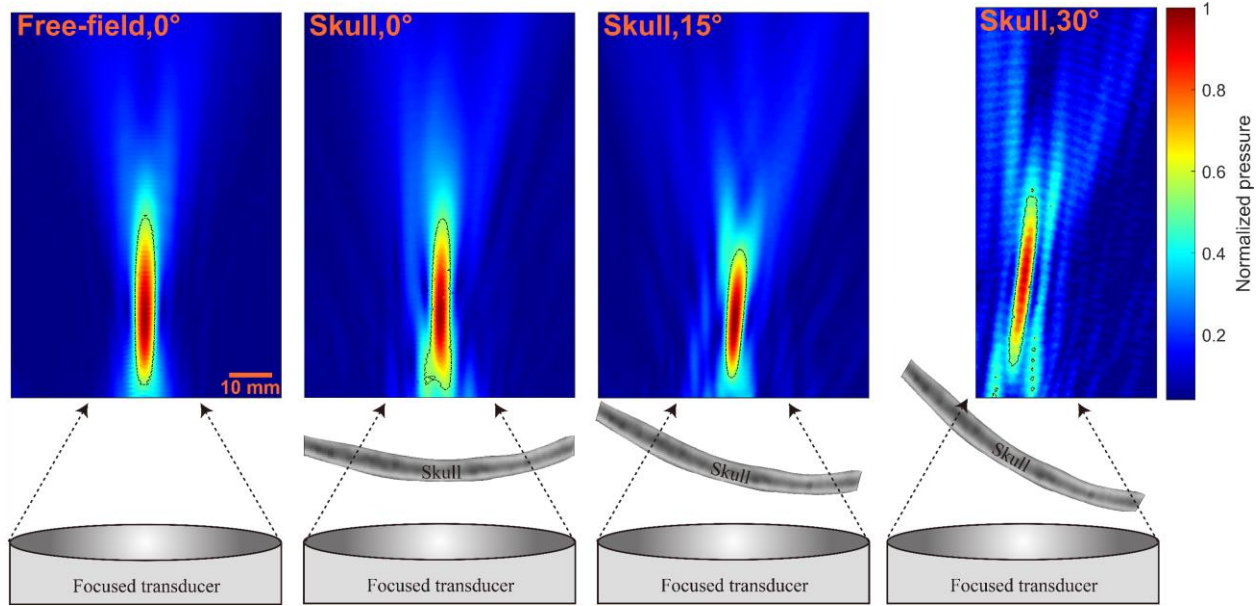


FIG. 8. (Color online). Acoustic field visualization of the 650kHz transducer beam profile in free-field and with the presence of a representative skull (thickness of 6.2 mm, SDR of 0.54, and RoC of 56.1 mm) at approximate angulation of  $0^\circ$ ,  $15^\circ$  and  $30^\circ$  to the right side of the transducer aperture. Pressure is normalized to its maximum value, the area enclosed by the dashed circle is where the pressure is above -6 dB of the peak pressure.

#### IV. DISCUSSION

To accurately capture acoustic field variations during sonication, limits were set on the temporal and spatial scope of data acquisition. The mapped transverse planes extended across at least twice the FWHM of the free-field focus. This provided adequate data collection in instances of focus shift or expansion, but also allowed field mapping to be completed within an hour. The pulse duration was set to approximately 0.5 ms. Though typical pulses delivered in in-person trials can extend to 20 ms,<sup>4</sup> 0.5 ms is long enough for the characteristics of continuous-wave sonication to develop.

The selected historical ROIs spanned a comprehensive range of characteristics. Thicknesses ranged from 3.1 mm to 12.5 mm, SDR from 0.07 to 0.75 and RoC from 26.8 mm to 113.0 mm. The Thiel ROIs examined were limited to thicknesses of between 5.3 mm to 12.2 mm, SDR values between 0.48 and 0.7, and RoC values between 15.4 mm and 114 mm. By using different ROIs across the two Thiel samples, we were able to reveal similarities and differences between transmission across historical and embalmed specimens.

#### **A. Transcranial focused ultrasound transmission**

As illustrated in FIG. 3, compared to the free-field, the foci shifts from center were 5.8 mm at 220 kHz, 7.8 mm at 650 kHz and 7.8 mm at 1000 kHz. The focal area increased compared to that of free-field by a factor of 1.1 at 220 kHz, a factor of 3.3 at 650 kHz, and a factor of 1.3 at 1000 kHz. For 220 kHz, at phase= $0^\circ$  and  $\pi/2$ , the errors between the two overlapping grids under the S1-focal area were 23.3% and 21.7%. For 650 kHz and 1000 kHz, due to a larger shift in focal position, the pressure and phase in the S1-focal area significantly deviate from the free-field reference, resulting in errors of 76.8% and 68.0% at peak pressure, and 26.0% and 15.6% at ambient pressure, respectively. The overall phase error over a full-cycle vibration is 20.9% at 220 kHz, 53.4% at 650 kHz and 46.4% at 1000 kHz.

The results presented in TABLE II show average transcranial peak pressure attenuations of 3.1 dB at 220 kHz, 9.0 dB at 650 kHz, and, and 14.6 dB at 1000 kHz. The average transcranial power attenuation demonstrated a less than square relationship to the pressure attenuation, of 5.0 dB, 14.9 dB, and 24.1 dB, respectively. These findings may be evidence of dispersion of the acoustic energy, attributable to scattering due to insertion angle, and the porous trabecular bone, which also contributed to an increase in the focal area by a factor of 1.1, 1.3, and 1.5 at the corresponding frequencies. As illustrated in FIG. 3 (a), in a normalized scenario, the area enclosed in the dashed line and its surrounding area both distributed more energy than the free-field- indicating that, in

practice, a sonication may affect more brain tissue than intended in order to produce the same level of pressure at the brain target.

The average transcranial phase error was 15.2%, 15.4%, and 23.8% at the three frequencies, respectively. For context, the phase error in the free-field maps was in the range of 5%-8%. Such variations might stem from measurement inaccuracies, however, empirically, errors below averaged value typically exhibited insignificant deviation from the free-field. This assertion is corroborated by the average focus shift results, which indicates the displacement of peak pressure relative to the free-field focus: 2.1 mm, 0.9 mm, and 0.7 mm at the respective frequencies. Notably, these shifts remained below half of the wavelength, and were maintained within the FWHM distance to the geometric focus at each frequency.

FIG. 4 illustrates the attenuation level of pressure and power at 220 kHz. These were observed to be within the ranges of -0.6 dB to -6 dB, and -1.0 dB to -11.0 dB, respectively, relative to free-field values. These attenuation levels appeared to be independent of thickness variations as indicated by the relatively flat linear fit. At 650 kHz, the transmitted pressure and power level displayed attenuation ranging from -6.4 dB to -13.9 dB, and -7.3 dB to -23.4 dB, respectively. The correlation between these attenuation levels and thickness (TH, mm) was discernible, and fitting revealed the linear regression equations:

$$p_{650kHz} = -0.5TH - 5.6 \pm 2.8, (R^2 = 0.30)$$

$$P_{650kHz} = -0.8TH - 9.3 \pm 6.0, (R^2 = 0.28)$$

Where  $p$  and  $P$  are pressure and power level, respectively. At the higher frequency of 1000 kHz, the transmitted pressure and power level were experienced further attenuation ranging from -7.5 dB to -22.6 dB, and -14.2 dB to -34.3 dB, respectively. Moderate correlations with thickness were evident, as expressed by the equations:

$$p_{1000kHz} = -1.4TH - 5.1 \pm 5.5, (R^2 = 0.54)$$

$$P_{1000kHz} = -2.2TH - 9.4 \pm 8.2, (R^2 = 0.56)$$

Notably, the data collected from the Thiel ROIs mostly fell within the confidence intervals at all three frequencies.

Similar patterns were also observed concerning the correlations between SDR and the attenuation. As shown in FIG. 5, at 220 kHz, the attenuation level of pressure and power exhibiting independence from variations in SDR, whereas weak correlations were noted at both 650 kHz and 1000 kHz:

$$p_{650kHz} = 5.7SDR - 11.3 \pm 2.7, (R^2 = 0.45)$$

$$P_{650kHz} = 10.9SDR - 19.3 \pm 5.3, (R^2 = 0.44)$$

$$p_{1000kHz} = 12.2SDR - 19.4 \pm 6.3, (R^2 = 0.40)$$

$$P_{1000kHz} = 18.9SDR - 31.5 \pm 9.6, (R^2 = 0.42)$$

The Thiel results aligned with the confidence intervals at 220 kHz and 650 kHz, whereas several deviations were apparent at 1000 kHz.

Conversely, as shown in FIG. 6, assessing the sharpness of the focus, at 220 kHz, the focal area varying between a factor of 0.9 to 2.0 to the free-field, demonstrating a moderate correlation with the skull curvature (RoC, mm):

$$F_{220kHz} = 8.710^{-3}RoC \pm 0.3, (R^2 = 0.54)$$

Where  $F$  is the intracranial focal area normalized to free-field. However, the focal area varied by a factor of 0.9 to 1.7 for 650 kHz and by 0.9 to 1.9 for 1000 kHz, with no discernible correlation to the skull curvature. The data from Thiel specimens fell within the 95% interval of the historical skull data.

The data shown in section III.C were measured at the distance where the pressure reached local maxima. The upper bound of the confidence interval can be used as a reliable indicator for

predicting the maximum possible intracranial pressure and power under specific conditions of skull thickness and SDR.

Using a 10 mm thick skull as an example, our linear regression fit models as demonstrated above indicate minimum peak pressure attenuation of 1.2 dB, 7.8 dB, and 13.6 dB, along with power attenuations of 1.8 dB, 11.3 dB, and 23.2 dB at frequencies of 220 kHz, 650 kHz, and 1000 kHz, respectively. The attenuation of the peak pressure at 1000 kHz falls below the estimated threshold of 14.5 dB<sup>20</sup> absorption loss through insertion of the skull. The attenuation at 220 kHz is even below the reflection coefficient of 4.8 dB.<sup>35</sup>

Consequently, should these linear fits be utilised to deliver continuous narrowband waveform for transcranial sonication, the upper bound of the confidence interval should be used for planning as a precautionary measure to mitigate the risk of excessive energy delivery to the target.

### **B. Impact of skull anatomy on transcranial transmission**

This experiment primarily focused on examining general transcranial FUS performance, rather than performance when engaging with a specific brain region. Multiple locations were tested on each calvarium, including the frontal, parietal and partially covers the temporal bones. As illustrated in FIG.1 and TABLE I, four regions, separated by the groove for superior sagittal sinus and coronal sutures were selected.

The R1 region, situated within the frontal bone, are generally characterized by their thickness ( $7.7 \pm 2.6$  mm), but it also features a smooth outer surface and comparable RoC ( $54.6 \pm 10.5$  mm) to the transducer. In practice, waves propagating through this region exhibited minimal focus shift and phase aberration. However, two ROIs within the R1 region featuring a bulging inner table, with a curved outward inner surface, resulted in an erroneous calculated inward curvature (RoC of 15.4 mm and 19.8 mm). The transmitted sound beam exhibited significant phase aberration at all three frequencies, prompting their exclusion from the group analysis.

The R2 region is located on the superior parietal bone, which is thin ( $6.4\pm 1.9$  mm) compared to other regions of the skull, except for the temporal window. However, the RoC ( $80.3\pm 17.5$  mm) is generally larger than in other regions, meaning this bone acted as a diffuser for the sound beam, resulting in a relative lowered peak pressure and broader coverage volume, particular evident at 220 kHz. Four ROIs from this region with a curvature greater than 100 mm, demonstrated a transmitted beam focal area over 35% larger than transmitted from its other regions at all three frequencies. These results were therefore not included in the analysis due to the observed distortion.

The R3 region is positioned on the lateral of the parietal bone and temporal bone. Although the structures in this region are on average the thinnest ( $5.8\pm 1.9$  mm), the irregularities of the surfaces and strong curvature ( $48.5\pm 12.6$  mm) contributed to greater phase aberration, reducing the transmission efficiency. Three ROIs from this region with a curvature less than 30 mm, exhibited 21%-41% lower transmitted pressure compared to ROIs with comparable thickness and SDR of that skull specimen. One ROI involving with the squamosal suture, with a thickness standard deviation of 2.1 mm, the transmitted pressure was dropped 44% to 56% for three frequencies compared to an adjacent location excluding the squamosal suture with the same mean thickness and a thickness standard deviation is 0.6 mm. Consequently, these ROIs were not considered ideal for transmission. However, challenges in these regions could potentially be mitigated by implement a relatively small transducer for transmission solely through the temporal window or using a phased array transducer to perform the phase correction.

The R4 region, located at the posterior of the parietal bone, had ROIs with a relatively smaller RoC ( $51.2\pm 7.7$  mm) compared to the RoC of the transducers, this often results in which acting as a confocal lens for the sound beam. This configuration reduced acoustic dispersion, enabling precise and even tighter focus field control. Results from transmission through this region were overall satisfactory, with none of the ROI were excluded from analysis.

### C. Impact of angulation and wave superposition on the transmitted pressure level

FIG. 8 shows the angulation effect on the resultant acoustic field at 650 kHz, the maximum beam depth and width above -6 dB is 37.0 mm and 4.0 mm in free-field- this is the same as when the skull piece was aligned normal to the beam. The depth and width are reduced to 28.0 mm and 3.5 mm at a relative angulation of 15° and 36.5 mm and 3.0 mm at a relative angulation 30°. The propagation direction appeared to be shifted by angulation of the ROI by 5° for a 15° angulation and by 7° for a 30° angulation. The peak intracranial pressure in the acoustic field with the skull piece at 0° and 15° were reduced to -9.8 dB and -10.8 dB of the free-field, respectively, and located close to the geometrical focus. Increasing the incident angle to 30° led to a peak pressure drop of -28.0 dB and shifted the focus 8.0 mm from the geometrical focus.

These results shown in FIG. 8 demonstrate the importance of keeping the ROI near normal to the transducer aperture, to avoid excessive phase aberration or excitation of shear modes. When employing a coupling medium, typically water or ultrasound gel, which has a significantly lower acoustic impedance to both the skull and transducer, the reflection coefficient at the interface of the media often exceeds 40%<sup>35,36</sup> and 90%,<sup>36</sup> respectively.

As shown in FIG. 7, concerning a representative skull ROI (thickness of 3.2 mm, SDR of 0.65, and RoC of 70.0 mm), significant interference effects are evident at 220 kHz and 650 kHz. The recorded intracranial peak pressure exhibited an oscillation pattern as the transducer-skull spacing increased from 10 to 50 mm. The pressure difference between the waveforms exhibiting constructive and destructive interference is approximately 30% to 40% at 220 kHz and 650 kHz. This effect was mitigated at 1000 kHz, with much lower pressure variation of roughly 10%. The linear fitted results demonstrated a decreasing trend as spacing increased. Specifically, the average pressure reduction for each 10 mm increment was observed to be approximately 2.0%, 3.5%, and 5.0% at 220 kHz, 650 kHz, and 1000 kHz, respectively.

This phenomenon is prominent across the sub-MHz frequency domain and is contingent upon the specific skull morphology. To mitigate standing wave effects, options could include chirped waveforms, random phase-shifting, or using phased-array transducers,<sup>12,37</sup> however, none of these are universal solutions for narrow-bandwidth, single-element transducers that most studies working with. Our experiment did not utilise intact skulls, therefore we provide no quantification of standing wave effects within the intracranial domain.

Our findings strongly indicate that wave superposition effects must be accounted for during FUS delivery to allow for FUS dose at the focal point to be accurately estimated. We have not measured the temperature throughout the experiment, as pressure levels are considerably lower than the safety level proposed by International Transcranial Ultrasonic Stimulation Safety and Standards (ITRUSST).<sup>38</sup>

#### **D. Future work**

Efforts were undertaken to integrate brain phantoms with the Thiel skull for the comprehensive transmission efficiency assessment. Using CT scans, the inner geometry of the Thiel calvaria was converted to a mesh and used to 3D print a mold. Polyvinyl alcohol-based brain phantoms were prepared by following the recommended procedure.<sup>39</sup> The prepared phantom has a sound speed of 1520 m/s and an attenuation coefficient of  $0.62 \pm 0.11$  dB/cm/MHz in the sub-MHz frequency, these parameters are comparable to the reported human brain parameters, which are 1530 m/s and  $0.58 \pm 0.35$  dB/cm/MHz<sup>1,3,40</sup> However, we were unable to overcome challenges in sealing the skull plus phantom system in the timeframe of this experiment, and this is the subject of ongoing work.

As previously mentioned, this experiment primarily focused on examining general transcranial FUS performance. An area of future study would be to assess theoretical target engagement via mapping space within the skull cavity to brain regions, as quantitative experimental treatment of how FUS engages both spatially and temporally with brain targets would be of use to the field.

## V. CONCLUSION

Comprehensive acoustic field mapping was conducted at frequencies of 220 kHz, 650 kHz and 1000 kHz, the outcomes revealed that the transmitted energy does not correlate to the skull thickness and SDR at 220 kHz, while weakly to moderately correlated at 650 kHz and 1000 kHz. Regarding the size of focal area, a moderate correlation with the skull curvature was observed at 220 kHz, with no discernible correlation at 650 kHz and 1000 kHz. Effects of wave superposition occurring at both transducer-skull spacing and within the skull thickness were noticed during experimentation and investigated. We found transmission across ROIs with large variations of thickness, and curvature below 30 mm and above 100 mm resulted in substantial field distortion across all tested frequencies, whereas transmitting from regions included in our analysis resulted in focus shift within half of the wavelength. Angulation between the skull and transducer beyond  $15^\circ$  should be avoided. Linear fitted models based on the skull thickness and SDR, along with a 95% confidence interval were provided at all three frequencies, notably, the thickness model demonstrated satisfactory accuracy at all frequencies tested, while the SDR model exhibited reduced efficacy at 1000 kHz. These models serve as useful tools for the determination of the output power levels in FUS treatment planning, therefore, enhancing the precision and efficacy in the therapeutic applications. Notably, the data collected from the Thiel ROIs mostly fell within the confidence intervals at all three frequencies indicating that testing on historical skulls yields data that may be valuable for in-human studies.

## ACKNOWLEDGMENTS

Thanks to Tom Gilbertson & Sadaquate Khan at the University of Dundee for helpful discussion, to Alan Webster for significant CT acquisition technical expertise, and to Michelle

Cooper facilitating the use of the skull specimens from the Centre for Human Anatomy and Identification (CAHID) at the University of Dundee.

## **AUTHOR DECLARATIONS**

### **Conflict of Interest**

The authors have no conflicts of interest to disclose.

### **Ethics Approval**

Approval for the use of human tissue specimens in the study was given by the University of Dundee Thiel Advisory group. This research complies with the Anatomy Act (1984) and the Human Tissue (Scotland) Act 2006.

## **DATA AVAILABILITY**

The data that support the findings of this study are available on request from the corresponding author. The data are not publicly available due to ethical restrictions.

## **REFERENCES**

<sup>1</sup> J. Kubanek, “Neuromodulation with transcranial focused ultrasound,” *Neurosurg Focus* **44**(2), (2018).

<sup>2</sup> A. Fomenko, C. Neudorfer, R.F. Dallapiazza, S.K. Kalia, and A.M. Lozano, “Low-intensity ultrasound neuromodulation: An overview of mechanisms and emerging human applications,” *Brain Stimul* **11**(6), 1209–1217 (2018).

<sup>3</sup> W. Legon, L. Ai, P. Bansal, and J.K. Mueller, “Neuromodulation with single-element transcranial focused ultrasound in human thalamus,” *Hum Brain Mapp* **39**(5), 1995–2006 (2018).

- <sup>4</sup> S.N. Yaakub, T.A. White, J. Roberts, E. Martin, L. Verhagen, C.J. Stagg, S. Hall, and E.F. Fouragnan, “Transcranial focused ultrasound-mediated neurochemical and functional connectivity changes in deep cortical regions in humans,” *Nat Commun* **14**(1), (2023).
- <sup>5</sup> H. Baek, K.J. Pakk, and H. Kim, “A review of low-intensity focused ultrasound for neuromodulation,” *Biomed Eng Lett* **7**(2), 135–142 (2017).
- <sup>6</sup> S.T. Brinker, F. Preiswerk, P.J. White, T.Y. Mariano, N.J. McDannold, and E.J. Bubrick, “Focused Ultrasound Platform for Investigating Therapeutic Neuromodulation Across the Human Hippocampus,” *Ultrasound Med Biol* **46**(5), 1270–1274 (2020).
- <sup>7</sup> V. Braun, J. Blackmore, R.O. Cleveland, and C.R. Butler, “Transcranial ultrasound stimulation in humans is associated with an auditory confound that can be effectively masked,” *Brain Stimul* **13**(6), 1527–1534 (2020).
- <sup>8</sup> C.R. Butler, E. Rhodes, J. Blackmore, X. Cheng, R.L. Peach, M. Veldsman, F. Sheerin, and R.O. Cleveland, “Transcranial ultrasound stimulation to human middle temporal complex improves visual motion detection and modulates electrophysiological responses,” *Brain Stimul* **15**(5), 1236–1245 (2022).
- <sup>9</sup> W. Lee, H. Kim, Y. Jung, I.U. Song, Y.A. Chung, and S.S. Yoo, “Image-guided transcranial focused ultrasound stimulates human primary somatosensory cortex,” *Sci Rep* **5**, (2015).
- <sup>10</sup> N. Samuel, M.Y.R. Ding, C. Sarica, G. Darmani, I.E. Harmsen, T. Grippe, X. Chen, A. Yang, N. Nasrkhani, K. Zeng, R. Chen, and A.M. Lozano, “Accelerated Transcranial Ultrasound Neuromodulation in Parkinson’s Disease: A Pilot Study,” *Movement Disorders* **38**(12), 2209–2216 (2023).

- <sup>11</sup> J.L. Sanguinetti, S. Hameroff, E.E. Smith, T. Sato, C.M.W. Daft, W.J. Tyler, and J.J.B. Allen, “Transcranial Focused Ultrasound to the Right Prefrontal Cortex Improves Mood and Alters Functional Connectivity in Humans,” *Front Hum Neurosci* **14**, (2020).
- <sup>12</sup> S. Yoo, D.R. Mittelstein, R.C. Hurt, J. Lacroix, and M.G. Shapiro, “Focused ultrasound excites cortical neurons via mechanosensitive calcium accumulation and ion channel amplification,” *Nat Commun* **13**(1), (2022).
- <sup>13</sup> T. Kirchner, C. Villringer, and J. Laufer, “Evaluation of ultrasound sensors for transcranial photoacoustic sensing and imaging,” (2023).
- <sup>14</sup> G. Pinton, J.F. Aubry, E. Bossy, M. Muller, M. Pernot, and M. Tanter, “Attenuation, scattering, and absorption of ultrasound in the skull bone,” *Med Phys* **39**(1), 299–307 (2012).
- <sup>15</sup> J. Guo, X. Song, X. Chen, M. Xu, and D. Ming, “Mathematical Model of Ultrasound Attenuation With Skull Thickness for Transcranial-Focused Ultrasound,” *Front Neurosci* **15**, (2022).
- <sup>16</sup> T.S. Riis, T.D. Webb, and J. Kubanek, “Acoustic properties across the human skull,” *Ultrasonics* **119**, (2022).
- <sup>17</sup> S. Pichardo, V.W. Sin, and K. Hynynen, “Multi-frequency characterization of the speed of sound and attenuation coefficient for longitudinal transmission of freshly excised human skulls,” *Phys Med Biol* **56**(1), 219–250 (2011).
- <sup>18</sup> J. Lee, D.-G. Paeng, and K. Ha, “Attenuation of the human skull at broadband frequencies by using a carbon nanotube composite photoacoustic transducer,” *J Acoust Soc Am* **148**(3), 1121–1129 (2020).

- <sup>19</sup> A.Y. Ammi, T.D. Mast, I.H. Huang, T.A. Abruzzo, C.C. Coussios, G.J. Shaw, and C.K. Holland, “Characterization of Ultrasound Propagation Through Ex-vivo Human Temporal Bone,” *Ultrasound Med Biol* **34**(10), 1578–1589 (2008).
- <sup>20</sup> F.J. Fry, and J.E. Barger, *Acoustical Properties of the Human Skull* (n.d.).
- <sup>21</sup> P.J. White, G.T. Clement, and K. Hynynen, *Local Frequency Dependence in Transcranial Ultrasound Transmission* (n.d.).
- <sup>22</sup> C.W. Connor, and K. Hynynen, “Patterns of thermal deposition in the skull during transcranial focused ultrasound surgery,” *IEEE Trans Biomed Eng* **51**(10), 1693–1706 (2004).
- <sup>23</sup> J.-F. Aubry, O. Bates, C. Boehm, K. Butts Pauly, D. Christensen, C. Cueto, P. G elat, L. Guasch, J. Jaros, Y. Jing, R. Jones, N. Li, P. Marty, H. Montanaro, E. Neufeld, S. Pichardo, G. Pinton, A. Pulkkinen, A. Stanziola, A. Thielscher, B. Treeby, and E. van ’t Wout, “Benchmark problems for transcranial ultrasound simulation: Intercomparison of compressional wave models,” *J Acoust Soc Am* **152**(2), (2022).
- <sup>24</sup> K. Hynynen, and F.A. Jolesz, “Demonstration of Potential Noninvasive Ultrasound Brain Therapy Through an Intact Skull,” *Ultrasound Med Biol* **24**(2), 275–283 (1998).
- <sup>25</sup> H. Niels, “Thirty years of Thiel embalming—A systematic review on its utility in medical research,” *Clinical Anatomy* **35**(7), 987–997 (2022).
- <sup>26</sup> *Human Tissue (Scotland) Act 2006* (n.d.).

- <sup>27</sup> K.W.K. Tsai, J.C. Chen, H.C. Lai, W.C. Chang, T. Taira, J.W. Chang, and C.Y. Wei, “The Distribution of Skull Score and Skull Density Ratio in Tremor Patients for MR-Guided Focused Ultrasound Thalamotomy,” *Front Neurosci* **15**, (2021).
- <sup>28</sup> A. Boutet, D. Gwun, R. Gramer, M. Ranjan, G.J.B. Elias, D. Tilden, Y. Huang, S.X. Li, B. Davidson, H. Lu, P. Tyrrell, R.M. Jones, A. Fasano, K. Hynynen, W. Kucharczyk, M.L. Schwartz, and A.M. Lozano, “The relevance of skull density ratio in selecting candidates for transcranial MR-guided focused ultrasound,” *J Neurosurg* **132**(6), 1785–1791 (2020).
- <sup>29</sup> M. D’Souza, K.S. Chen, J. Rosenberg, W.J. Elias, H.M. Eisenberg, R. Gwinn, T. Taira, J.W. Chang, N. Lipsman, V. Krishna, K. Igase, K. Yamada, H. Kishima, R. Cosgrove, J. Rumià, M.G. Kaplitt, H. Hirabayashi, D. Nandi, J.M. Henderson, K.B. Pauly, M. Dayan, C.H. Halpern, and P. Ghanouni, “Impact of skull density ratio on efficacy and safety of magnetic resonance–guided focused ultrasound treatment of essential tremor,” *J Neurosurg* **132**(5), 1392–1397 (2020).
- <sup>30</sup> ISO/IEC, “IEC 62127-1 Ultrasonics - Hydrophones - Part 1: Measurement and characterization of medical ultrasonic fields,” (2013).
- <sup>31</sup> ISO/IEC, “IEC 62127-2 Ultrasonics - Hydrophones - Part 2: Calibration for ultrasonic fields up to 40 MHz,” ISO/IEC, (2007).
- <sup>32</sup> ISO/IEC, “IEC 61828 Ultrasonics - Transducers - Definitions and measurement methods regarding focusing for the transmitted fields,” ISO/IEC, (2020).
- <sup>33</sup> ISO/IEC, “IEC 61689 Ultrasonics - Physiotherapy systems - Field specifications and methods of measurement in the frequency range 0,5 MHz to 5 MHz,” ISO/IEC, (2022).

- <sup>34</sup> ISO/IEC, *Ultrasonics – Power Measurement – Radiation Force Balances and Performance Requirements* (2006).
- <sup>35</sup> D.N. White, G.R. Curry, and R.J. Stevenson, *THE ACOUSTIC CHARACTERISTICS OF THE SKULL* (Pergamon Press, 1978).
- <sup>36</sup> V.T. Rathod, “A review of acoustic impedance matching techniques for piezoelectric sensors and transducers,” *Sensors (Switzerland)* **20**(14), 1–65 (2020).
- <sup>37</sup> S.C. Tang, and G.T. Clement, “Standing-wave suppression for transcranial ultrasound by random modulation,” *IEEE Trans Biomed Eng* **57**(1), 203–205 (2010).
- <sup>38</sup> J.-F. Aubry, D. Attali, M. Schafer, E. Fouragnan, C. Caskey, R. Chen, G. Darmani, E.J. Bubrick, J. Sallet, C. Butler, C. Stagg, M. Klein-Flügge, S.-S. Yoo, B. Treeby, L. Verhagen, and K. Butts Pauly, *ITRUSST Consensus on Biophysical Safety for Transcranial Ultrasonic Stimulation* (n.d.).
- <sup>39</sup> S. Taghizadeh, C. Labuda, and J. Mobley, “Development of a Tissue-Mimicking Phantom of the Brain for Ultrasonic Studies,” *Ultrasound Med Biol* **44**(12), 2813–2820 (2018).
- <sup>40</sup> F. Duck, *Physical Properties of Tissues: A Comprehensive Reference Book* (Academic press, 2013).